JOURNAL OF GEOPHYSICAL RESEARCH, VOL. 115, F02016, doi:10.1029/2009JF001390, 2010

Variation of deposition depth with slope angle in snow avalanches: Measurements from Vallée de la Sionne

Betty Sovilla,[1] Jim N. McElwaine,[2] Mark Schaer,[1] and Julien Vallet[3]

Received 13 May 2009; revised 27 November 2009; accepted 8 January 2010; published 10 June 2010.

[1] The snow surface height was precisely measured, with a laser scanner, before and after the passage of two dry-mixed avalanches in Vallée de la Sionne during the winter of 2005–2006. The measurements were used to calculate the depth of the deposited snow along each entire avalanche path with a height resolution of 100 mm and a horizontal resolution of 500 mm. These data are much more accurate than any previous measurements from large avalanches and show that the deposit depth is strongly negatively correlated with the slope angle. That is, on steep slopes the deposit is shallow, and on gentle slopes the deposit is deep. The time evolution of the snow depth, showing the initial erosion and final deposition as the avalanche passed, was also observed at one position using a frequency-modulated continuous wave radar. Measurements at a nearby position gave flow speed profiles and showed that the avalanche tail consists of a steady state subcritical flow that lasts for about 100 s. Eventually, the tail slowly decelerates as the depth slightly decreases, and then it comes to rest. We show that the dependency between the slope angle and the deposition depth can be explained by both a cohesive friction model and the Pouliquen h_{stop} model.

Citation: Sovilla, B., J. N. McElwaine, M. Schaer, and J. Vallet (2010), Variation of deposition depth with slope angle in snow avalanches: Measurements from Vallée de la Sionne, *J. Geophys. Res.*, *115*, F02016, doi:10.1029/2009JF001390.

1. Introduction

[2] The determination of entrained and deposited masses is crucial to understanding the dynamics of snow avalanches. However, while entrainment processes have been recently investigated [*Sovilla et al.*, 2001, 2006; *Gauer and Issler*, 2004], there has been almost no work on avalanche deposition processes, and in both cases there has been little comparison between observations and theory, even though laboratory, theoretical, and numerical analyses have been carried out by numerous research groups [*Pouliquen*, 1999; *Félix and Thomas*, 2004; *Tai and Kuo*, 2008; *Naaim et al.*, 2003].

[3] Previous measurements of snow erosion and deposition were performed using manual or photogrammetric methods. Manual methods [*Sovilla et al.*, 2001] give estimates of both eroded and deposited depths, but they are difficult to apply in hazardous areas such as avalanche couloirs, have poor spatial resolution, and are extremely time consuming. Photogrammetry [*Vallet et al.*, 2001] can give data without risk, but its high cost means that it has been used only sporadically and not over the whole avalanche path. The data are expensive both to collect and to process. In addition, the poor contrast of the snow surface and the frequent destruction of the necessary ground control points by avalanches limit photogrammetry.

[4] Since beginning in the winter season of 2005–2006, aerial laser scanning has complemented photogrammetric measurements of snow cover depth at the Vallée de la Sionne avalanche test site, which is located in the western part of Switzerland [*Ammann*, 1999]. Laser scanning allows the automatic calculation of a high-resolution and accurate digital surface model of the snow. No ground control points are necessary, and the accuracy is independent of the contrast of the snow. Measurements can be taken of the entire avalanche path with a horizontal spatial resolution of 500 mm and a vertical accuracy of 100 mm. The data points have much higher resolution and are more homogeneous than previous photogrammetric measurements, which only measured the release and deposition zones and had a resolution of 2–3 m and an accuracy of 100–150 mm in high-contrast areas and 300–500 mm in low-contrast areas [*Vallet et al.*, 2001]. The measurement and data analysis procedures are described in detail in section 2, which also describes the test site.

[5] In section 3 we present the laser scanner measurements from two dry-mixed avalanches (Figure 1). We also compare these spatial measurements with temporal measurements from frequency modulated continuous wave (FMCW) radar along with internal speed profiles to gain insight into the deposition process. In section 4 we discuss the results and compare the deposition depth with two simple models.

[6] The two studied avalanches are dry-mixed avalanches. They consist of a dense flowing layer supported by direct

[1]WSL Institute for Snow and Avalanche Research SLF, Davos, Switzerland.
[2]Department of Applied Mathematics and Theoretical Physics, University of Cambridge, Cambridge, UK.
[3]Ulrich,Wiesmann and Rolle, Epalinges, Switzerland.

0148-0227/10/2009JF001390

Figure 1. Avalanche 816. (top) Typical dry-mixed avalanche artificially released at the Vallée de la Sionne test site. (bottom) The deposit left by a dry-mixed avalanche on a steep slope shows a homogeneous snow depth distribution.

particle-particle contacts. This layer lies beneath a suspension layer, where the snow particles are supported by turbulent eddies in the air. In between, there can be a gradual transition through a saltation layer [*Issler*, 2003] or a sharp interface. This work concentrates on erosion and deposition from the basal layer and concentrates in particular on deposition occurring on the main part of the avalanche track, where the slope is still relatively steep (greater than 20°). Deposition on slopes steep enough to sustain flow is typically much more homogeneous (Figure 1, bottom) than deposition on shallower slopes in the runout zone. Here steady flow is not possible, and often there results a much more complicated structure with repeated surges laying down many separate layers.

2. Study Site and Experimental Methods

[7] Vallée de la Sionne is the location of the Swiss full-scale avalanche experimental site. It is close to the town of Sion, in the western part of Switzerland [*Ammann*, 1999; *Issler*, 1999]. Avalanches start from three main release areas, indicated in Figure 2 with the abbreviations PR (Pra Roua), CB1 (Crêta Besse 1), and CB2 (Crêta Besse 2), and follow a partially channeled track. The runout zone starts immediately below the channeled area, where a debris cone extends to the valley bottom. Large avalanches may partially climb the slope on the opposite side of the valley.

[8] Crêta Besse 1 is the steepest release zone (Figure 3). During the winter season, frequent small avalanches start naturally and stop immediately below the release zone or in the westerly channel. Crêta Besse 2 and Pra Roua are less steep. Spontaneous avalanches from these release zones are less frequent.

[9] Instrumented obstacles are located on a debris cone about 200 m below the channeled area (Figures 2 and 3). At this location, sensors measure speed, impact pressure, and air pressure in the avalanche body [*Sovilla et al.*, 2008a; *Kern et al.*, 2009; *McElwaine and Turnbull*, 2005]. Density measurements are performed at 3 and 6 m above ground [*Louge et al.*, 1997]. Seismic sensors [*Vilajosana et al.*, 2007] and FMCW radars [*Gubler and Hiller*, 1984] are installed at three locations along the avalanche path.

[10] Remote measurements of speed are also performed with Doppler radars installed in a bunker facing the avalanche paths [*Rammer et al.*, 2007] and with terrestrial photogrammetry [*Vallet et al.*, 2004]. The latter method is also used to determine the volume of the avalanche powder cloud. Helicopter-based photogrammetry [*Vallet et al.*, 2001] has been used to map snow cover depths before and after the passage of an avalanche in order to calculate the avalanche mass balance [*Sovilla et al.*, 2006].

[11] Since 2005–2006, laser scanning and photogrammetry have been combined in a single sensor unit operated from a helicopter to measure the snow surface height. The sensors are integrated with a direct georeferencing system, eliminating the need for ground control points. The camera is a digital Hasselblad H1D with 22 megapixel resolution. The laser scanner is a Riegl LMS-Q240i that measures 10,000 points s^{-1} (22 lines of 455 points). It works by measuring the travel time of laser pulses scanned across the surface by a rotating polygonal mirror. The direct georeferencing system combines an inertial measurement unit (iMAR FSAS) with a dual-frequency GPS receiver. The measurements are linked to the national coordinate frame using a GPS reference station. The system can be orientated obliquely to the slope to reduce errors.

[12] The data from the laser scanner are an unstructured three-dimensional set of points. They are mapped onto a Cartesian grid with 0.5 m spacing and the heights interpolated at each vertex. A moving average of 10 × 10 cells (5 m × 5 m) was then applied to reduce local errors.

[13] To determine the net erosion and deposition of the snow cover, the surface is mapped before, z_1, and after, z_2, the avalanche. A complete map of the surface altitude, z_s, is also made during summer when there is no snow. The snow depth before the avalanche can thus be calculated by subtracting the summer measurement from the measurement before the avalanche:

$$h_s = z_1 - z_s. \tag{1}$$

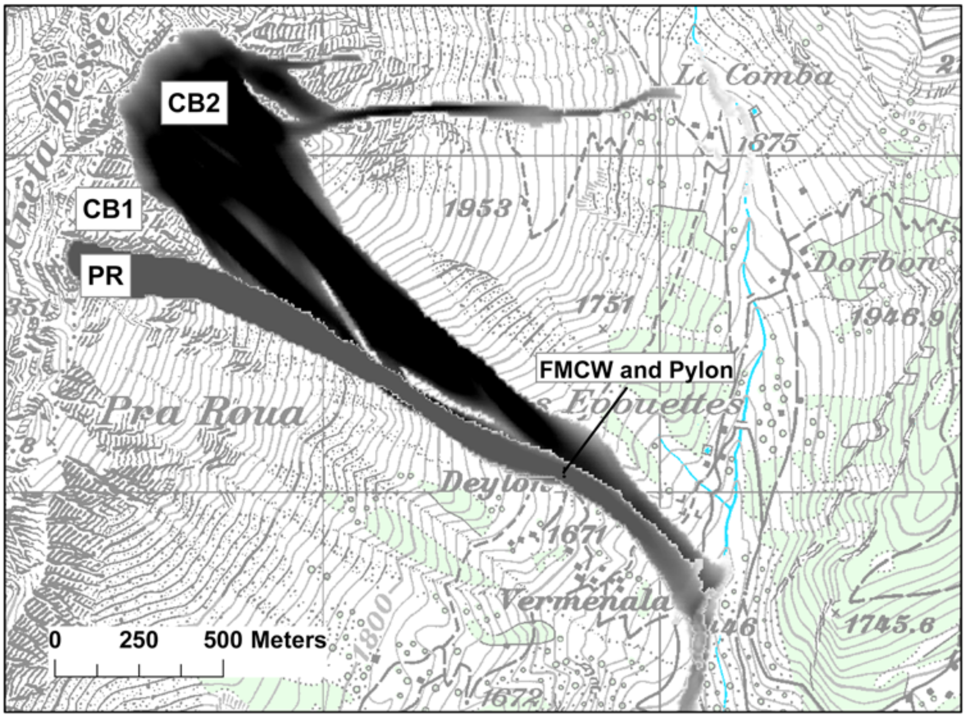

Figure 2. Overview of the Vallée de la Sionne test site. The release zones Pra Roua (PR), Crêta Besse 1 (CB1), and Crêta Besse 2 (CB2) are marked. The shaded regions represent the typical paths followed by avalanches released from Pra Roua and Crêta Besse 2. The top right corner of the map is at latitude 46°18′ 26.33″N and longitude 7°23′11.52″E.

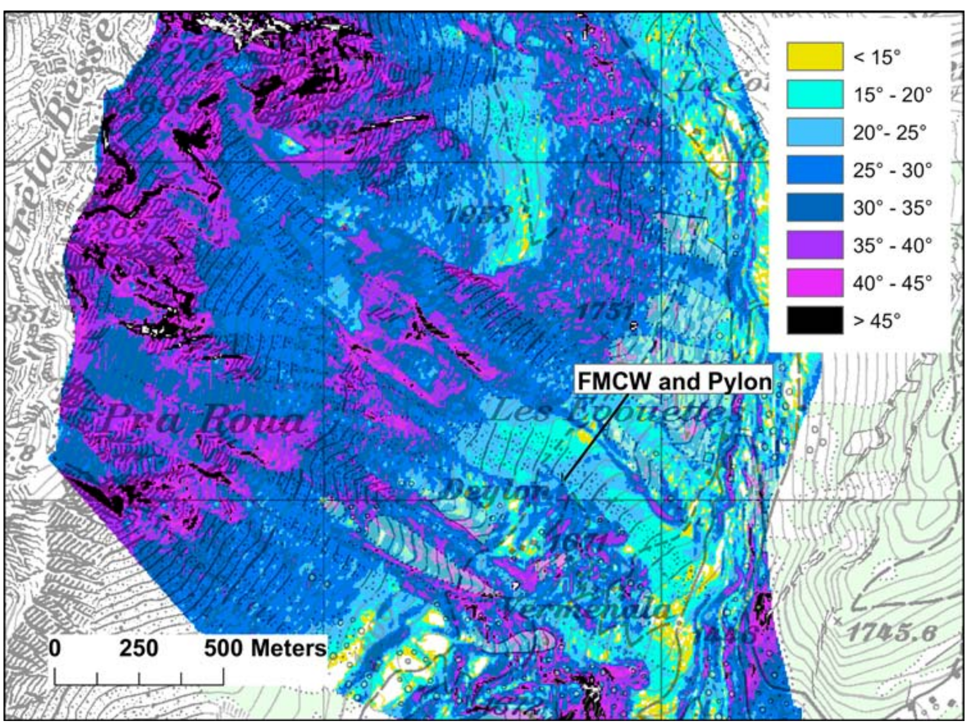

Figure 3. Slope angles of the Vallée de la Sionne test site.

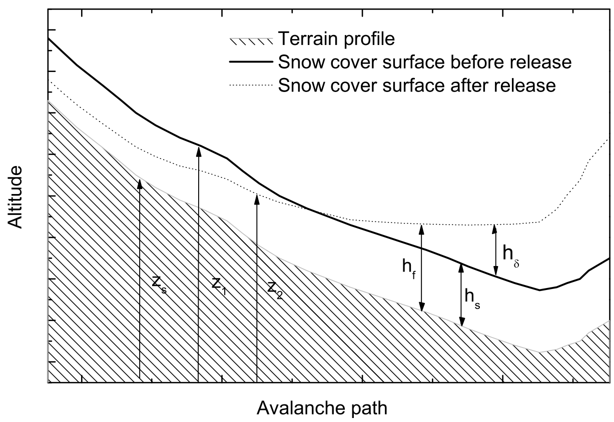

Figure 4. Laser scanner measurement: definition of variables. The variables are measured vertically.

[14] The snow depth after the passage of the avalanche is calculated similarly:

$$h_f = z_2 - z_s. \tag{2}$$

The net erosion and deposition can be calculated by subtracting these two depths directly or by subtracting the altitudes:

$$h_\delta = h_s - h_f = z_1 - z_2 = h_e - h_d, \tag{3}$$

where h_e is the depth of snow eroded and h_d is the depth of snow deposited. Only the difference between h_e and h_d, h_δ, can be calculated separately from the laser scanner measurements; h_e and h_d cannot be calculated separately. The height and depth variables are all measured vertically, and their definitions are shown in Figure 4.

[15] Since we are primarily interested in changes in snow depth, we only consider relative errors, and these are smaller than the absolute errors. The accuracy of the snow cover depth measurements is impaired by several effects. The precision of the laser scanner is specified as 20 mm (standard deviation) at 50 m range. At this distance the spot averages over a region of 132 mm. At larger distances the precision decreases. At 300 m the precision of the laser scanner is estimated to be 30–40 mm (standard deviation).

[16] The starting zone was flown over in parallel, oblique strips, while the rest of the area was measured while flying along the avalanche track with the helicopter at 300 m above ground, with a flying speed of 15 m s^{-1}. Therefore, we estimate the range error relative to the helicopter to be better than 50 mm, where the ground surface is well defined and smooth. However, the precision of the summer measurements without snow has much larger errors, up to 1000 mm, because parts of the deposition area are covered by bushes and trees. This implies that while h_δ is accurate to around 100 mm, h_s and h_f can be much less accurate depending on the slope position. At a height of 300 m the laser spot is 795 mm wide, and the point spacing is around 1.5 points m^{-1} in both horizontal directions. The surface scans contain 400,000–700,000 points depending on the helicopter flight path.

[17] The second source of errors is due to the calculation of the absolute position of the laser scanner from the GPS-IMU system. To minimize these errors, the same GPS reference station, located at Arbaz, was always used to compute the trajectory of the system during the mapping. The GPS reference has been aligned with the national reference frame (LV95) using the Automated Global Navigation Satellite System Network for Switzerland (AGNES) permanent GPS network stations. The estimated absolute accuracies for the positions and the orientation angles of the sensor are 40 mm for the X and Y positions, 50 mm for Z, 0.5 arc min (0.008°) for the roll and pitch angle, and 1.5 arc min (0.025°) for the azimuth. This implies point cloud errors of 50–60 mm in all directions, so the final error in absolute point position is around 100 mm.

[18] The relative accuracy can be computed by differencing overlapping flight lines or by computing the differences between two sessions when the surface height has not changed. The average difference between common sections before and after the trigger is a few centimeters, while the standard deviation of the differences is 100 mm. Unchanged areas, i.e., areas not crossed by the avalanches, present an average difference of 15 mm, with a standard deviation of 110 mm (Figure 5).

3. Experimental Results

[19] We analyze two avalanches which were artificially released on 6 March 2006. We refer to these avalanches by their archive numbers, 816 and 817, to allow cross-reference with other publications. For the same avalanches see *Sovilla et al.* [2008b] for an analysis of avalanche impact pressures and *Kern et al.* [2009] for a study on shear rates and speed variations.

[20] Avalanche 816 was released from PR and part of CB1 following the approximate trajectory shown in Figure 2. Avalanche 817 was released 10 min later from CB2. The avalanche basal layers mostly followed separate tracks, while the powder clouds followed tracks that joined in the runout zone. Both avalanches were stopped by the counterslope.

[21] Laser scanning was performed before and after the two avalanches but not in between. This complicates the analysis because the basal layers of the two avalanches partially intersected (Figure 6). We exclude this area from our analysis. The powder clouds overlapped over all of the final part of the track, and it was not possible to separate their individual contributions. In this analysis we assume that the powder contribution to the deposition depth in the overlapping sections is negligible in comparison to the contribution from the basal layer (see also section 3.2).

[22] Note that for avalanche 816 (Figure 6, crosshatched area) some of the laser scanner data (Figure 6, dark gray area) are missing. This is because avalanche 816 moved out of the area that was measured before the avalanche was released.

3.1. Snow Cover Depth Before and After Release

[23] Snow cover depths before, h_s, and after, h_f, release were calculated from equations (1) and (2) and are shown in Figure 7. Note that some regions in the avalanche runout zone have negative depth. These data correspond to the forested regions along the avalanche path. Recall that because of digital terrain model errors in the forested areas, data precision decreases.

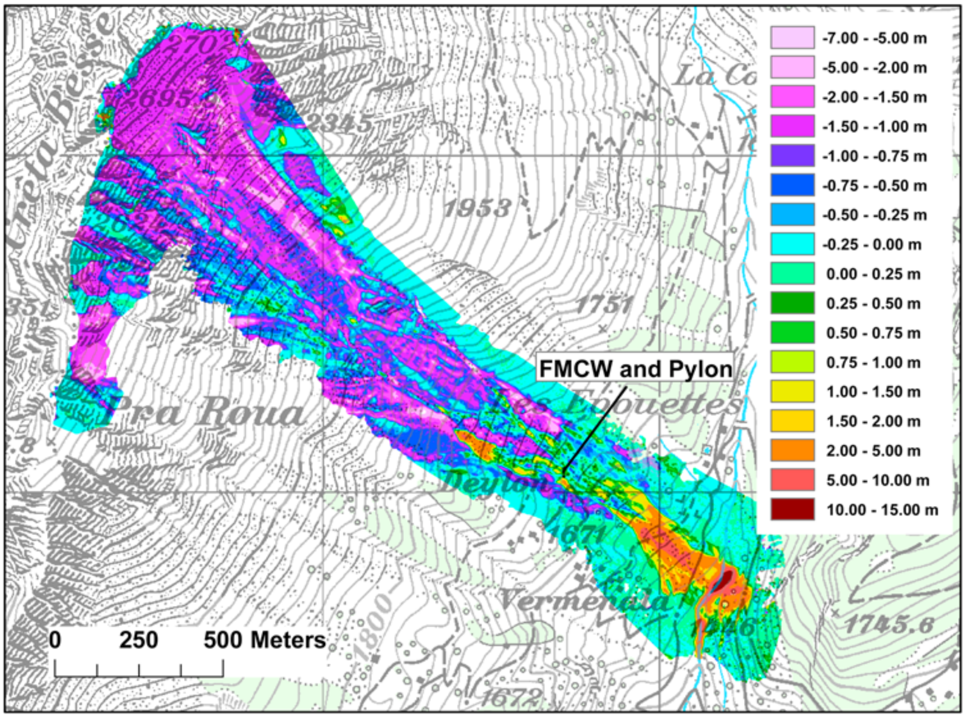

Figure 5. Snow depth variations, h_δ (difference in height before and after the release), measured with the laser scanner at the Vallée de la Sionne test site after the release of avalanches 816 and 817 (6 March 2006). Unchanged areas present an average difference of 15 mm, with a standard deviation of 110 mm.

[24] Figure 7 (top) shows the snow cover before release. We see that snow depths are extremely variable, being a complex function of topographical parameters such as altitude, exposition, and slope angle as well as depending on previous erosion and deposition processes by wind and other avalanches.

[25] During the winter season of 2005–2006 frequent snowfalls (Figure 8) were followed by intense avalanche

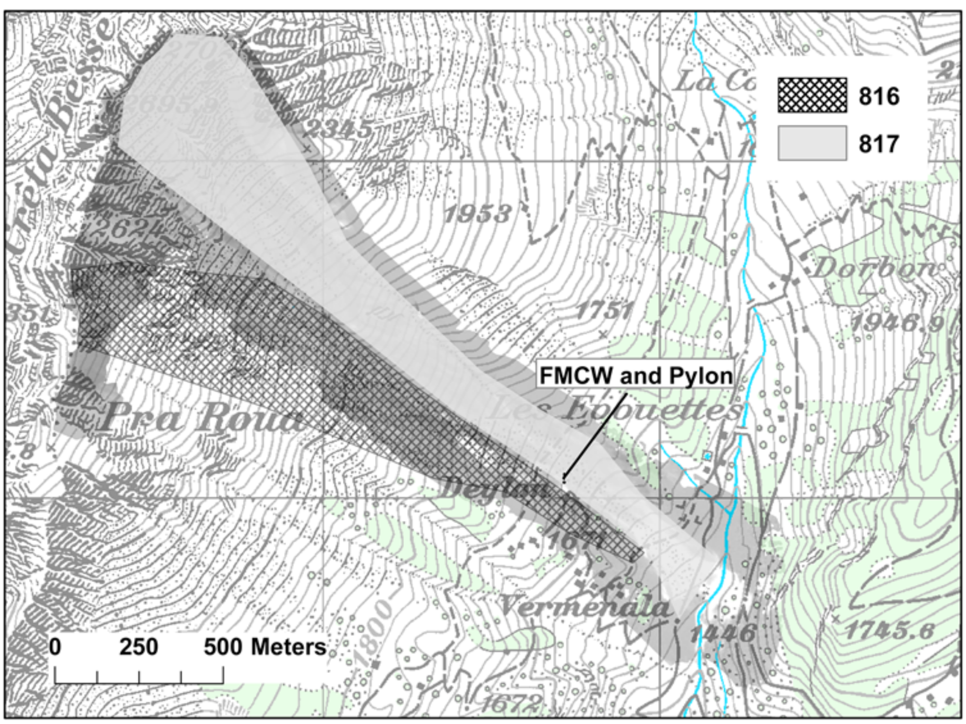

Figure 6. The area covered by laser scanner measurements (dark gray). The crosshatched area is the region analyzed for avalanche 816, and the light gray area is the region analyzed for avalanche 817.

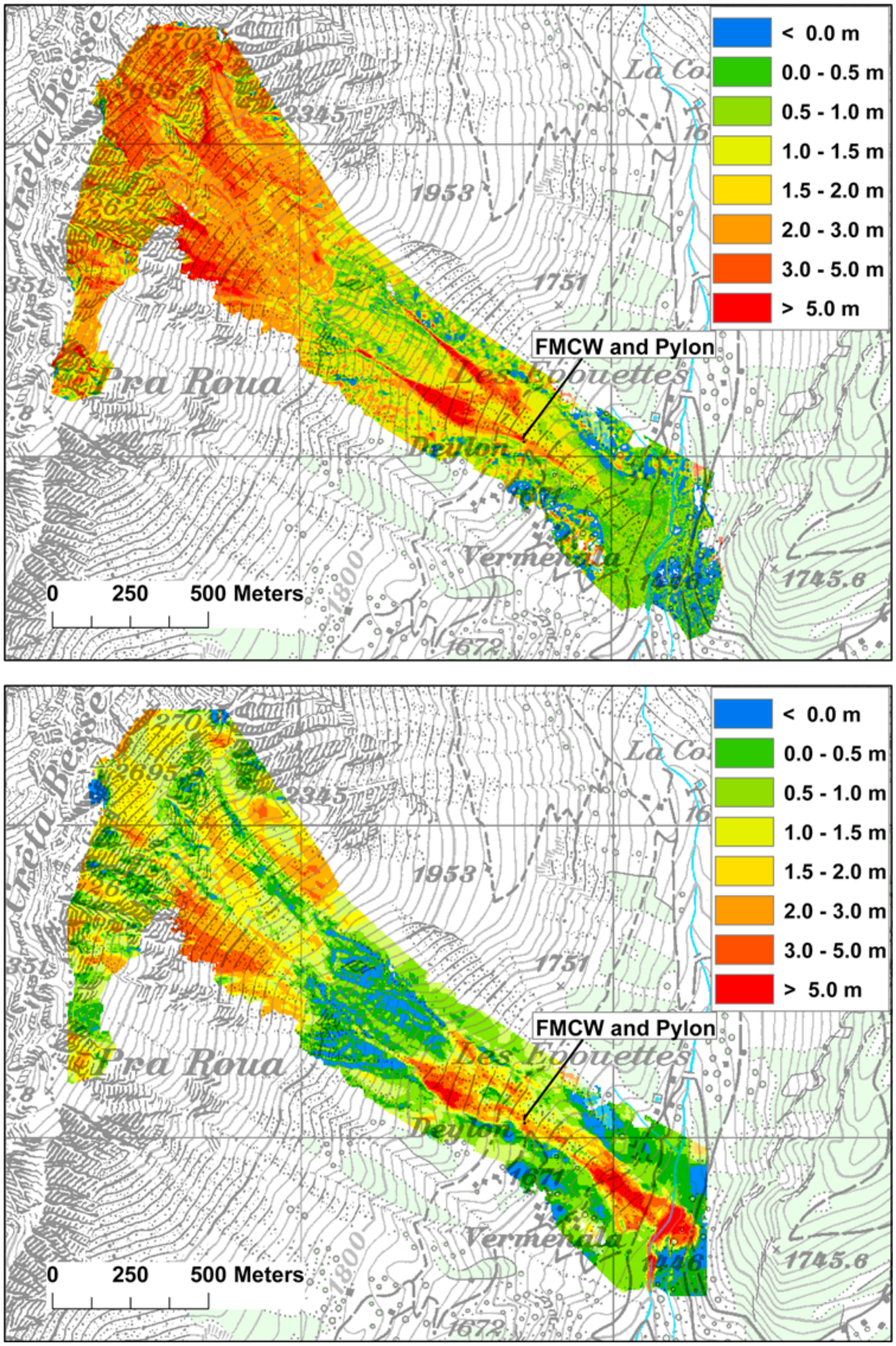

Figure 7. Snow cover depths (top) before, h_s, and (bottom) after, h_f, avalanches 816 and 817.

activity. Small avalanches naturally started from almost all release areas. The smallest of these stopped immediately below the release zone, while a few entered the channelized zone and reached the valley bottom (Figure 7, top). These naturally released avalanches were monitored by linear synthetic aperture radar (LISA), installed at the site in the winter season of 2003–2004 [*Martinez-Vazquez and Fortuny-Guasch*, 2006]. None of these avalanches reached the obstacle zone; however, they contributed to the removal of part of the snow cover from the steepest parts of the slope and its deposition on flatter areas.

[26] In 2006, between 1 and 5 March, 1200 mm of new snow fell (Figure 8). Between 2 and 4 March, the temperature increased by 12°C, and the snowline rose to over 2000 m above sea level (asl). On 3 and 4 March a spontaneous avalanche started from CB1 (Figure 2), moving some snow

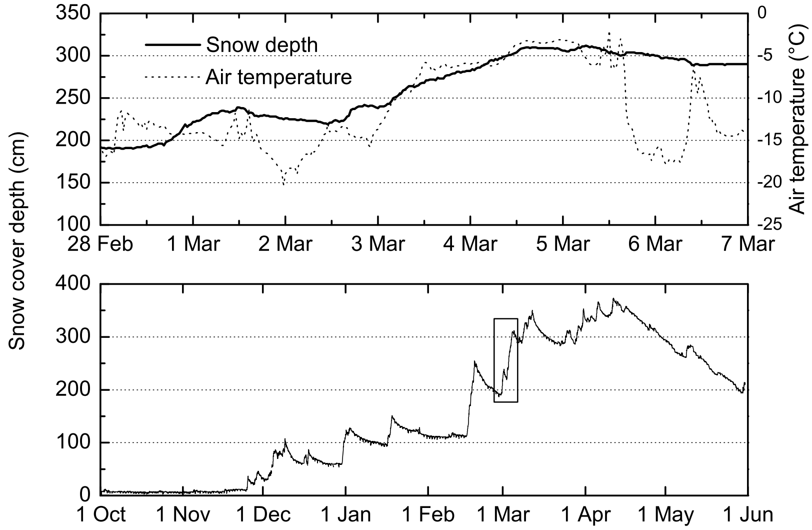

Figure 8. (top) Snow cover depth and air temperature in the week before the avalanche was released. (bottom) Snow cover depth during the winter season of 2005–2006. Data are from the meteorological station Donin du Jour, which is located at 2390 m asl, close to Vallée de la Sionne.

from the release zone and the track to the westerly channel. The temperature then dropped rapidly and stayed low until 6 March, when the weather cleared and we were able to artificially release avalanches 816 and 817.

[27] Figure 7 (bottom) shows the snow cover depths immediately after the second avalanche. Snow cover depths, h_f, have been calculated using equation (2). We see that not all of the snow cover was entrained by the avalanches, especially in the upper part of the track. Only the upper layer of the snow cover was released by the explosion. Large quantities of snow, which had been deposited by previous avalanches immediately below the release zone, were not entrained. However, all of the snow cover was entrained in the steeper part of the track between 1800 and 2000 m asl.

3.2. Snow Cover Depth Variations After the Avalanches

[28] The snow cover depth variations along the avalanche path, h_δ, the difference between erosion and deposition (equation (3)), are shown in Figure 5. Most deposition and erosion are due to the passage of the avalanche's dense basal layer, even though in the lower part of the track, the powder cloud covered almost the same area as the laser scanning measurements. This can be deduced by comparison with areas that the basal layer did not reach and where the deposition was only due to the powder cloud. Deposition depths in these areas were insignificant.

[29] Figure 9 shows the range of h_δ grouped by the slope angle for each grid point. The data have been divided into classes; the histograms beneath the box plots indicate the number of point measurements for each class. We excluded from the analysis data corresponding to slope angles larger than 45° and 46° and smaller than 16° and 21° for avalanches 817 and 816, respectively. Points for these slope classes are few and not statistically significant (Figure 9). Figure 3 shows slope angles of the Vallée de la Sionne test site and confirms that the excluded data are from isolated spots and are thus unimportant.

[30] While there is high variability at each slope angle, the mean values, $\overline{h}_\delta$ (Figure 9, squares in boxes), follow a clear

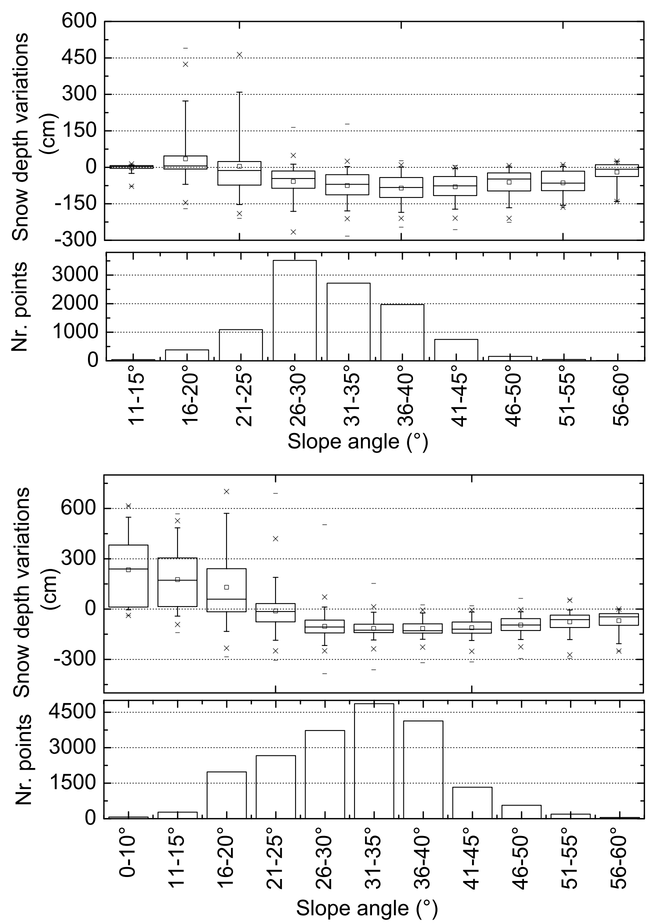

Figure 9. Snow cover depth, h_δ, for different slope classes: (top) avalanche 816 and (bottom) avalanche 817. The box plots show the mean (squares in boxes), median (lines in boxes), 25% and 75% percentiles (boxes), 5% and 95% percentiles (whiskers), and 0% and 100% percentiles (crosses). Histograms show the number of points in a class.

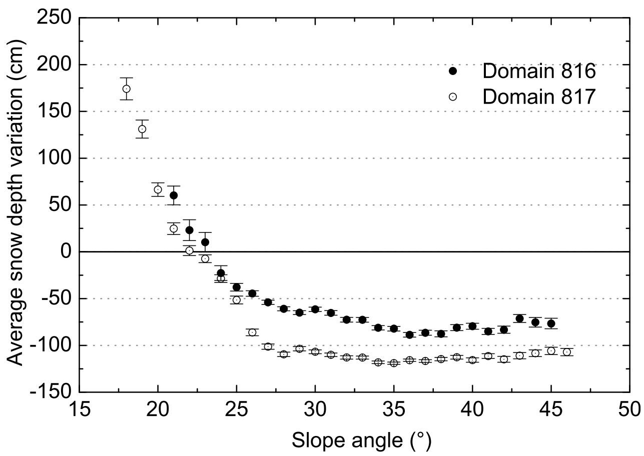

Figure 10. Average snow depth variation, $\overline{h}_\delta$, as a function of slope angle for avalanches 816 and 817. Only slope angles where avalanche data are statistically significant are shown.

trend. Figure 10 shows $\overline{h}_\delta$ as a function of slope angle for the two avalanches. There is a strong correlation between average snow cover depth variations and slope angle for both avalanches. Note that the curves are similar in form, and at slope angles above 35°, they are shifted by an approximately constant value.

3.3. Entrainment and Deposition Estimation

[31] During an avalanche we expect that over most of the track, snow is first eroded and then deposited. The measurement $\overline{h}_\delta$ combines these two processes according to

$$\overline{h}_d = \overline{h}_\delta + \overline{h}_e, \tag{4}$$

where $\overline{h}_e$ is the average erosion depth. Therefore, to investigate $\overline{h}_d$ in detail it is necessary to estimate the erosion along the avalanche path.

3.3.1. Entrainment Depth Estimate

[32] Previous studies on snow entrainment show that entrainment is governed by the availability of snow mass along the avalanche path as well as by the structure of the snow cover. For example, a new snow layer is easily entrained, whereas an ice crust may prevent entrainment. Parametrizing mass uptake using topographic features (slope angle and surface roughness) or dynamical parameters (speed and flow depth) is of secondary importance in comparison to determining the snow cover structure since in many cases all available snow is entrained [*Sovilla et al.*, 2001, 2006]. Therefore, as a first approximation, the erosion depth is estimated to be equal to the depth of new snow along the avalanche path. The new snow accumulation is measured at the meteorological station Donin du Jour, located close to the avalanche path at an altitude of 2390 m asl. Figure 8 shows that at the time of the avalanche release there was around 1.10 m of new snow at 2390 m asl.

[33] To verify this value, a direct estimate of the average erosion depth, $\overline{h}_e$, can also be made from $\overline{h}_\delta$ measurements on steeper slopes, where avalanches do not deposit [*Sovilla et al.*, 2001]; that is, we assume that $\overline{h}_d = 0$ for slopes steeper than about 35°, and thus, equation (4) becomes $\overline{h}_e = \overline{h}_\delta$. Figure 10 shows that on slopes steeper than 35°, avalanche 817 entrained on average about 1.13 m of snow, with a maximum of 1.19 m. These values correspond approximately to the new snow precipitation measured at the weather station Donin du Jour (Figure 8). Avalanche 816 entrained about 0.82 m, with a maximum of 0.89 m. These lower values may be due to erosion by the 3 and 4 March avalanches, which entrained part of the new snow cover in the domain of avalanche 816.

[34] The entrainment depth can also be estimated by evaluating snow cover depths where erosion of the whole snow cover occurred. Figure 7 (bottom) shows that there is a large area where full erosion, but no deposition, occurred approximately between altitudes of 1800 and 2000 m asl, especially in the domain of avalanche 817. In the domain of avalanche 816 old deposits are still visible.

[35] For this area, Figure 11 shows a detailed analysis of the snow cover depth before release, $\overline{h}_s$, and corresponding snow cover depth variations, $\overline{h}_\delta$, as a function of altitude classes for the avalanche domains 816 and 817. Both avalanches entrained on average 0.95 m of snow. The lower value is attributed to the lower altitude since the snowfall limit was at about 2000 m asl. Figure 12 shows entrainment depths as a function of altitude.

3.3.2. Deposition Depth Estimate

[36] We assume that the deposition depth, h_d, is zero for slope angles larger than 35° where the snow depth variation remains approximately constant, as shown in Figure 10. For slopes less than 35°, we assume that $\overline{h}_e$ = 1.19 m for avalanche 817 and $\overline{h}_e$ = 0.82 m for avalanche 816, which corresponds to the erosion depth at 35°. Equation (4) can then be used to calculate the mean deposition, $\overline{h}_d$, from the data for $\overline{h}_e$ shown in Figure 12. We assume that the slightly different value of erosion below the altitude of 2000 m asl (Figure 12) is compensated for by the larger deposition depths at lower altitudes.

[37] Figure 13 shows deposition depths as a function of slope. Here $\overline{h}_d$ decreases monotonically to zero with

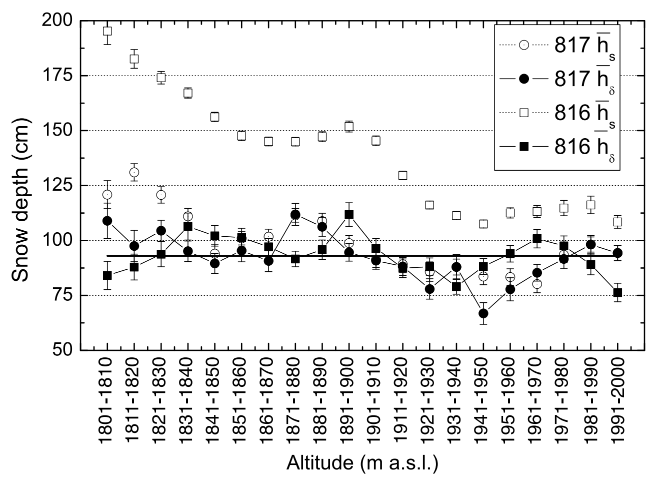

Figure 11. Average snow depth variation, $\overline{h}_\delta$, and snow cover depth, $\overline{h}_s$, prior to the avalanche release as a function of altitude classes in the domains of avalanches 816 and 817. The horizontal line represents the average $\overline{h}_\delta$ for both avalanche 816 and avalanche 817.

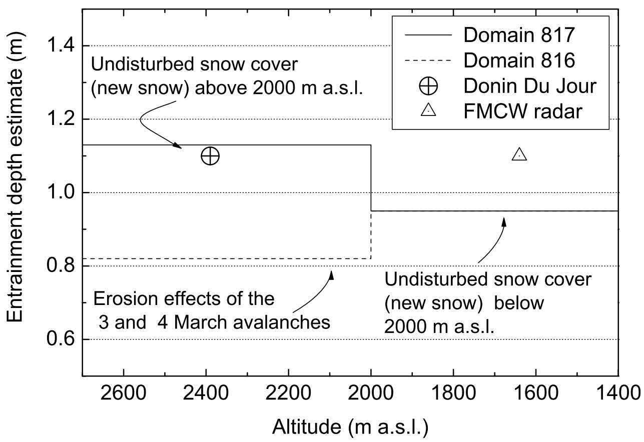

Figure 12. Entrainment depth estimate, h_e.

increasing slope angle. We see that the avalanches started to deposit on a slope angle of approximately 33° (note that with our assumptions $\overline{h}_d = 0$ by definition for slope angles greater than 35°). There appears to be a minimum deposition depth $\overline{d}_{\min}$ of the order of 0.05–0.1 m, but it is hard to draw conclusions about this as this is below the accuracy of our measurements and it depends strongly on our assumptions about $\overline{h}_e$.

3.4. Time-Dependent Observations of Erosion and Deposition

[38] The laser scanner measurements give the snow height before and after the passage of the avalanches over most of the track but yield no information about the time evolution of the snow cover. To complement this, we use FMCW radar data [*Gubler and Hiller*, 1984], which give the time evolution of the snow cover in the obstacle zone. The radar is located at an altitude of 1640 m asl, on a slope of about 21° (Figure 5). This is close to the 20 m pylon, where the flowing snow depth is measured with mechanical sensors and the speed profile is measured with optical sensors [*Tiefenbacher and Kern*, 2004]. The speed at different heights and the measured flow depths are shown in Figure 14 [*Kern et al.*, 2009].

[39] The FMCW radar points upward and measures continuously a vertical section of the avalanche. Reflections are generated by interfaces between layers with different properties such as density, water content, grain size, or grain shape. Figure 15 shows the amplitude of the reflected signal as a function of height from the surface and time. The boundary between the static snow cover and the flowing snow is clearly visible and shows how erosion and deposition vary with time.

[40] The horizontal lines in Figure 15 between 40 and 53 s show layer boundaries in the snow covering the radar before the avalanche arrives. At about 53 s, these lines are disrupted by the arrival of the avalanche. The avalanche entrains about 1.10 m of snow within 2 s and then slides over a surface located approximately 0.8 m above the ground. The surface gradually changes from an irregular, rough morphology (between 53 and 60 s) to a smoother and more regular surface (between 60 and 90 s). Toward the avalanche tail, from 90 s, we can see the formation of an ice layer (Figure 15, dark area). The ice layer may be formed by the high shear rate near the base generating heat, which melts the snow [*Kern et al.*, 2004, 2009].

[41] Figure 14 (top) and Figure 14 (middle) show speed measurements from inside the avalanche. The speeds are measured at fixed heights from the ground. Between 100 and 200 s the lower sensors were temporarily buried in a local deposit formed by the impact of the avalanche on the pylon; thus, we miss speed measurements in this time window. This temporary deposit disappears at around 200 s.

[42] Between 53 and 60 s the acceleration of the entrained snow produces a large shear in the speed profile in the avalanche head (Figure 14, top). Between 60 and 100 s there is no entrainment, and the internal shear decreases in time as the bottom surface is smoothed and an ice layer forms. From 100 to 265 s the surface is very smooth and icy. The avalanche flows as a plug over a narrow, basal shear layer [*Kern et al.*, 2009]. The plug-like flow lasts until deposition starts.

[43] Finally, Figure 14 (bottom) shows flow depths measured with slide switches at the pylon compared with those derived from FMCW radar. Slide switches are set at intervals of 250 mm along the pylon and open through contact with the moving snow particles. The highest sensor touched by the avalanche defines the avalanche flow depth. The signal is erratic because of the intermittent contact with snow clusters. We can see differences between the two measurements. They are due to both their different mechanisms of operation and the spatial variability of the avalanche flow. Recall that the pylon and FMCW radar are not at exactly the same location.

[44] Figure 14 shows that the flow depth decreases between 53 and 100 s and then remains approximately constant until 220 s. As the avalanche decelerates, the flow depth slowly decreases. Note that the depth decrease after 220 s is not visible on the FMCW plot.

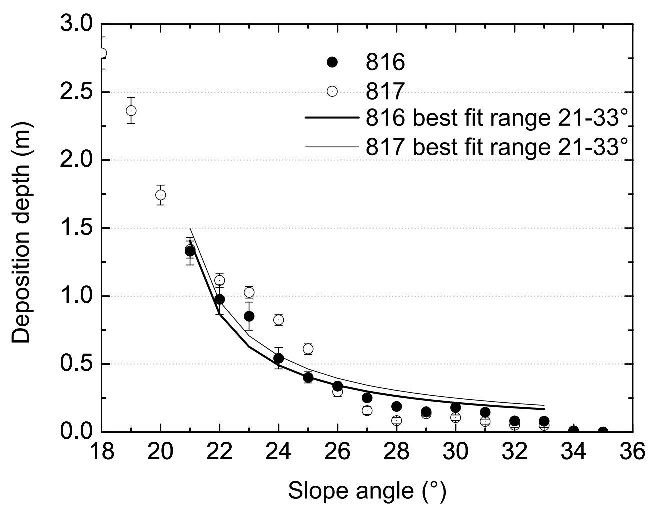

Figure 13. Deposit depth $d_f = h_d \cos\theta$ as a function of slope angle for avalanches 816 and 817. Lines show the cohesive-frictional model least squares fit.

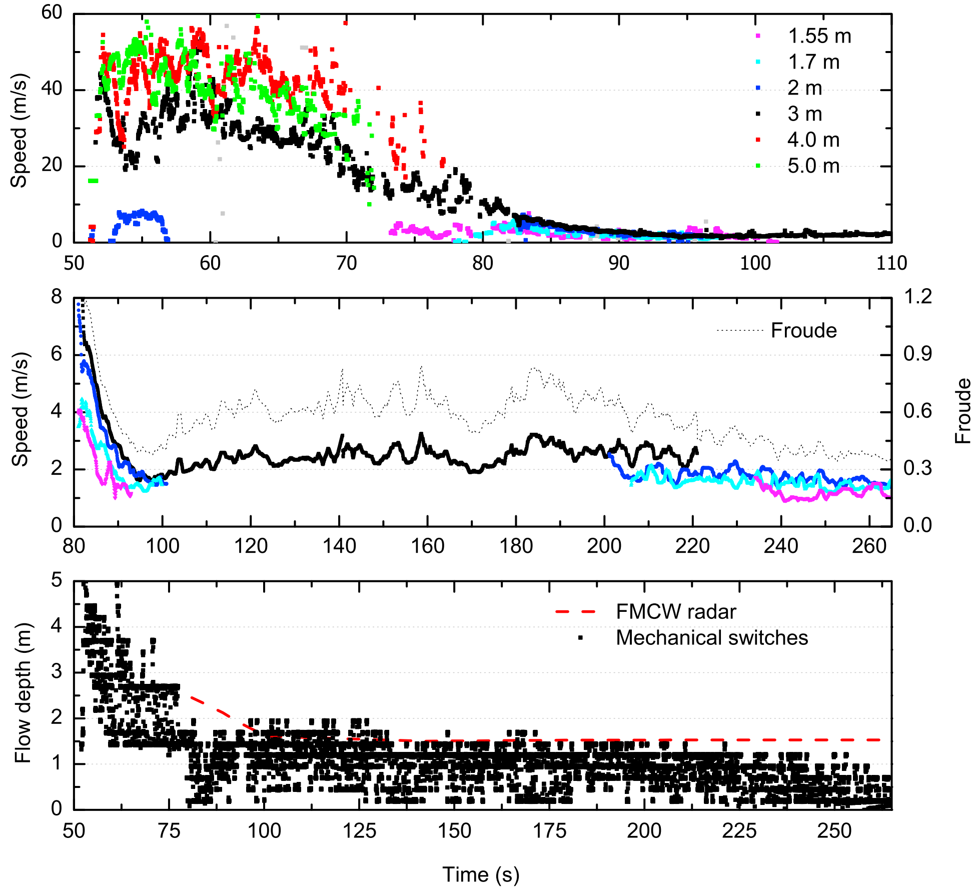

Figure 14. (top) Frontal speed measured at the pylon. (middle) Tail speed from avalanche 816 [*Kern et al.*, 2009]; Froude number is also plotted. (bottom) Flow depths for avalanche 816 measured with mechanical switches and derived from the FMCW radar measurements.

[45] The FMCW radar recording time was unfortunately limited to 265 s, a few seconds before the avalanche tail completely stopped, so we could not observe the entire deposition process. However, the measurements suggest that deposition occurs just when the flow depth decreases, after a long period of steady state with constant flow depth. We assume that there exists a critical depth, which is the minimum depth at which flow can occur for a given slope angle,

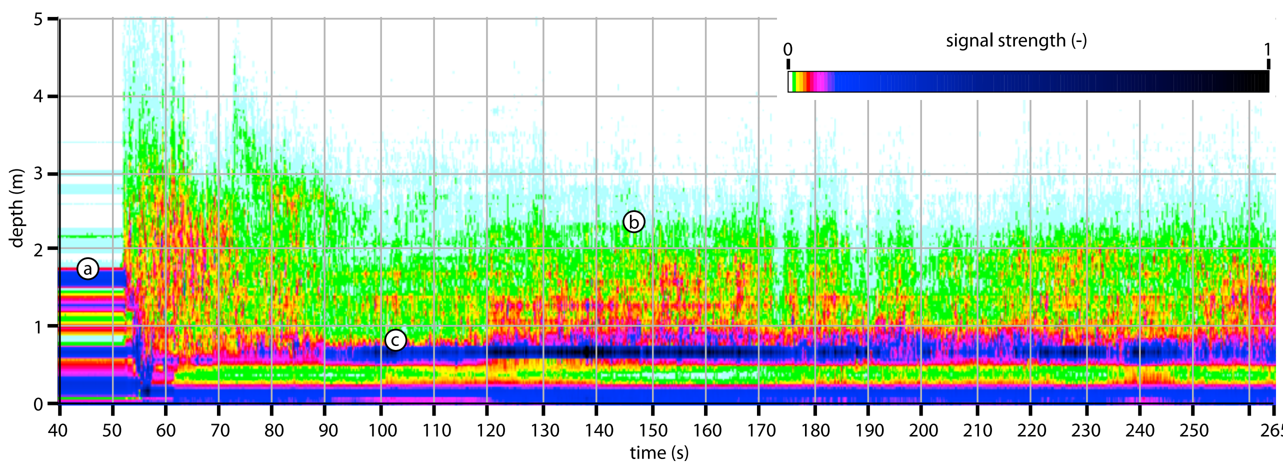

Figure 15. FMCW radar measurements from avalanche 816. The radar is located close to the obstacle zone at an altitude of 1640 m asl and on a slope of about 21°. Here a, b, and c correspond to the positions of the snow cover depth before and after release and the position of the sliding surface, respectively.

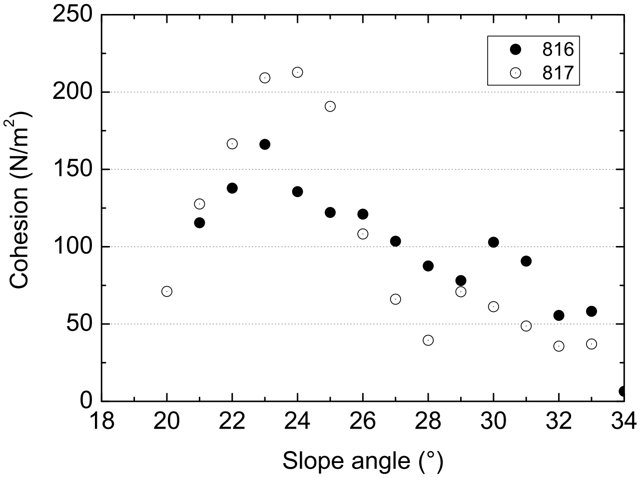

Figure 16. Cohesion stress c derived from equations (5) and (6) assuming μ = 0.35 and μ = 0.36 for avalanches 816 and 817, respectively, and ρ = 300 kg m^{-3}.

so when less mass is available at the tail of the avalanche the flow quickly stops at a similar depth.

4. Discussion

[46] In this section we will try to better understand the relationship between slope angle and deposition depth shown in Figure 13. We discuss two different approaches: a Mohr-Coulomb frictional model with cohesion and an empirical fitting curve as originally proposed by *Pouliquen* [1999].

[47] Deposition in the main part of the avalanche track occurs on slopes of 21°–33°. The deposition occurs after a long period of almost steady flow at low speed in a plug flow regime [*Sovilla et al.*, 2008a]. Plug flow regimes are characterized by a low shear rate, $\dot{\gamma}$, on the order of 1 s^{-1} or less [*Sovilla et al.*, 2008a; *Kern et al.*, 2009]. The low shear rate means that the snow particles are in continuous contact and that eventually cohesive forces may develop.

[48] The size distribution of the particles in the flowing snow may also play a role. Observations of deposit granulometry show that dry, dense avalanches are characterized by a lognormal granular size distribution, with a median granule size of approximately 70–120 mm [*Bartelt and McArdell*, 2009]. This polydisperse granular mixture is immersed in loose snow grains of a few millimeters in diameter. Both clusters and loose grains may form in the avalanche from a continuous breaking down and reforming of the clusters or may originate during entrainment. The formation process of the clusters cannot be observed during the flow, so it is not clear if this clusters-loose grain structure is always present or only forms just as the avalanche is stopping. Nevertheless, both clusters and loose grains are present in the depositing phase. Since a polydisperse mixture allows flows at higher packing fraction, the loose snow grains may act as cohesive bridges between clusters and may therefore favor the formation of enduring particle contacts.

4.1. A Cohesive-Frictional Deposition Model

[49] The retarding forces acting on avalanches arise from processes that are both complicated and disputed by avalanche experts. They may depend in detail on the structure of both the flowing snow and stationary snow cover, and there may also be inertial forces due to snow entrainment. However, near the avalanche tail, when the avalanche is slowing down and is very close to deposition, dynamic forces are negligible, so we assume that we can describe the drag force S by a simple Mohr-Coulomb frictional model with cohesion:

$$S = c + \mu N, \qquad (5)$$

where c is the cohesive force, μ = tan ϕ (where ϕ is the internal friction angle), and $N = \rho g d_f \cos\theta$ is the normal force. Here ρ is the avalanche density, d_f is the flow depth perpendicular to the ground (equal to $h_d \cos\theta$ in the deposit), θ is the slope angle, and g is the acceleration due to gravity. To leading order, for the shallow layer approximation, this retarding force must balance gravity, so

$$\rho g d_f \sin\theta = c + \mu\rho g d_f \cos\theta. \qquad (6)$$

This force balance implies that for each slope θ there is a characteristic snow depth d_f, for which the snow stops, given by

$$d_f = \frac{c}{\rho g(\sin\theta - \mu\cos\theta)} = \frac{c\ \cos\phi}{\rho g \sin(\theta - \phi)}. \qquad (7)$$

We used ρ = 300 ± 60 kg m^{-3} for the density in the tail, which we assumed to be constant. This choice was based on the analysis of density data derived from permittivity measurements performed inside the avalanche, 3 m above ground [*Louge et al.*, 1997]. On the basis of our experience, we estimate that the density measurement is accurate to within 20%. Note that typical deposition density for mixed avalanches at the Vallée de la Sionne ranges between 300 and 400 kg m^{-3} [*Sovilla et al.*, 2006].

[50] We calculated the least squares fit for the cohesion c and the friction angle $\phi = \tan^{-1}\mu$ for the measurements in the slope range 21°–33° for both avalanches using equation (7). We found c = 123 ± 25 N m^{-2} and μ = 0.35 ± 0.02 for avalanche 816 and c = 146 ± 26 N m^{-2} and μ = 0.36 ± 0.02 for avalanche 817.

[51] Because of uncertainties in the density measurements the estimates of cohesion have large errors, but this does not affect the estimates of μ. Nevertheless, both cohesion and μ turned out to be in rough agreement with cohesion and Coulomb friction data from snow chute experiments obtained by direct dynamics measurements of shear and normal stresses [*Platzer et al.*, 2007]. For dry avalanche flow, *Platzer et al.* [2007] were able to calculate an average cohesion of about c = 100 N m^{-2} and an average friction coefficient of about μ = 0.26. In these experiments the chute slope was 45°, the average snow density was just above 300 kg m^{-3}, and the flowing depth was approximately 0.50 m.

[52] Figure 13 shows that this simple model gives a good quantitative agreement with the data and describes well the observed correlation between deposition depth and slope angle. However, the accuracy of the fit decreases for high slope angles. This may partly be a problem with estimating the deposit depth because when this is low, small variations in the estimated entrainment depth may be critical. To study this further, we now consider cohesion to vary in equations (5)

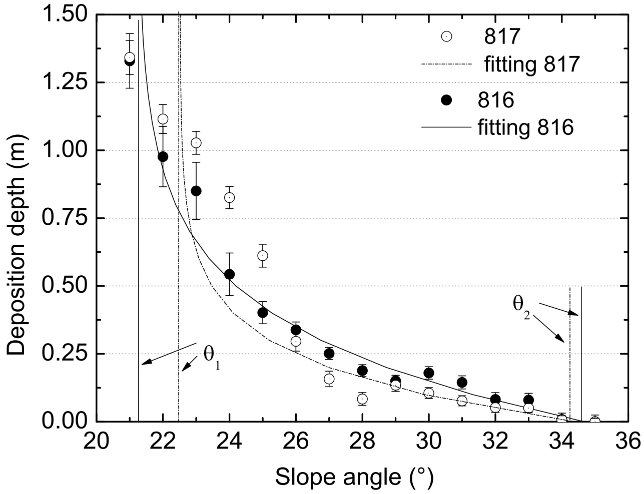

Figure 17. Deposit depth, $d_f = h_d\cos\theta$, fitted to the Pouliquen model (equation (8)). Parameters for avalanche 816 are θ_1 = 21.4°, θ_2 = 34.7°, and L = 0.31 m. Parameters for avalanche 817 are θ_1 = 22.5°, θ_2 = 34.4°, and L = 0.19 m.

and (6) as a function of slope angle, with μ and ρ being constant. The results are shown in Figure 16. Cohesion appears to decrease as slope increases, although the data are too uncertain to be sure of this trend. This trend may be due to higher speeds on steeper slopes, which is also related to the problem that this model predicts some deposition even on vertical slopes, whereas little deposition is seen on slopes over 34°. A possible explanation is that the cohesive forces will only come into effect if the avalanche moves sufficiently slowly, and on the steeper slopes this does not occur.

4.2. Pouliquen Model

[53] The relation between deposit depth and slope angle is remarkably similar to observations in granular flow experiments performed by *Pouliquen* [1999] and *Jop et al.* [2006] and the theory of *Jenkins* [2006]. *Pouliquen* [1999] performed dense granular flow experiments on steep slopes and observed that after closing the gate of the reservoir, the thickness of the flow decreased, and the flow slowed down, stopped, and left a static layer of material on the bed. Pouliquen defined the thickness of this layer as h_{stop}. In his interpretation, h_{stop} depends on the slope, the property of the material (particle size and geometrical trapping effects), and the roughness of the bed, but it is independent of the initial speed and height of the flow. The deposit depth left by avalanches 816 and 817 along the avalanche path agrees with this picture. It is measured in areas where the slope is relatively steep, that is, greater than 20°, where steady flow can be sustained, and depends primarily on the slope angle.

[54] *Pouliquen* [1999] proposed an empirical expression that he fitted to his data:

$$\tan\theta = \tan\theta_1 + (\tan\theta_2 - \tan\theta_1)\exp\left(-\frac{h_{\mathrm{stop}}}{L}\right), \qquad (8)$$

where θ_1 and θ_2 are angles. For $\theta < \theta_1$ static deposits of any depth are possible, and no steady flowing state exists. For $\theta > \theta_2$ flowing grains will never come to rest. $L = \alpha\, d$ is a length scale, where d is the particle diameter and α is a coefficient (typically 2–8). Equation (8) can be rearranged to give $h_{\mathrm{stop}} = L \log[(\tan\theta_2 - \tan\theta_1)/(\tan\theta - \tan\theta_1)]$. The three parameters are fitted to our data and are shown in Figure 17. For avalanche 816 we find θ_1 = 21.4°, θ_2 = 34.7°, and L = 0.31 m. For avalanche 817 we find very similar angles, θ_1 = 22.5° and θ_2 = 34.4°, but a rather different length scale, L = 0.19 m. If we take d = 100 mm [*Bartelt and McArdell*, 2009], this gives α in the correct range. However, relationship (8) has not been tested when there is such a large range of particle sizes. There are still single grains of d = 1 mm, and if this d were taken, an unrealistic α would result. Furthermore, it is not clear whether d = 100 mm clusters can exist in the flow or are merely transported on the surface. If the flow is shearing strongly, large clusters would probably be broken up. It may be that these large clusters can gradually form and grow once the shear rate is sufficiently low, that is, when the flow is nearly plug-like. The cluster size could gradually increase until the h_{stop} criterion is attained and the flow comes to rest.

5. Conclusions

[55] Our observations suggest that on steep slopes in the range 21° < θ <34°, deposition occurs at the avalanche tail when the flow depth decreases below a critical value, which depends on slope, sliding surface, particle characteristics, and flow density. The deposition depth is just a few centimeters less than the steady state flow depth that the system reaches in the subcritical flow regime at the avalanche tail. This suggests that deposition may occur not only at the tail but also in other parts of the avalanche where the flow depth is close to the critical depth. Thus, at the avalanche borders, where flow depths are usually smaller than in the middle of the flow, deposition processes may start first. This can also be a partial explanation for the formation of levees, which are frequently observed in the lower deposition zone, and it would be in agreement with granular flow experiments performed by *Félix and Thomas* [2004].

[56] For this range of inclinations, we can exclude two possible deposition mechanisms.

[57] 1. Deposition occurs as a gradual process from the bottom so that the basal surface slowly rises and the flow height decreases [*Kneller and Buckee*, 2000]; in fact, during deposition, the avalanche moves as a plug, and the speed decreases simultaneously everywhere in the flowing layer. Because we did not observe shearing, it is highly probable that the flow freezes more or less instantaneously because of frictional and cohesive forces throughout its depth.

[58] 2. The stopping mechanism is due to the formation of an upward propagating shock separating a stationary, deposited lower region from the rest of the still-moving avalanche. Obviously, this is not possible in the bulk of the flow and particularly in the tail, as they are subcritical (Figure 14, middle). In addition, there is no evidence for such a sharp transition region, which would involve a rapid increase in snow depth, but instead there is a gradual and slow change in the flow characteristics, so this can be excluded.

[59] We cannot exclude the possibility that shocks may form where the flow is still supercritical [*Gray et al.*, 2003]. The high deposition depths measured on slopes less than 21° may also be generated in a different manner. Shortly before the avalanche stops, deposition may be built up in several

stages by earlier deposits being successively overrun by later parts of the flow rather than by the avalanche coming to a stop simultaneously throughout its depth.

[60] We have shown that the deposit depth in the central part of the avalanche track is quantitatively described both by a simple cohesive-frictional model and by the Pouliquen h_{stop} model. Both models give similarly good fits, but the cohesive-frictional model has only two fitting parameters rather than three. We believe it also more accurately describes the underlying physics because cohesive forces are undoubtedly important. However, neither the cohesive-frictional model, which does not consider grain size effects, nor the Pouliquen approach, which does not consider cohesive forces, can completely explain the complex nature of deposition in avalanches. Additional complications include flow regime changes, time evolution of the basal surface, and metamorphism and aggregation of the flowing snow crystals as well as three-dimensional effects. Despite these complications we have shown how simple models can give insight into and understanding of field observations.

[61] Our observations are from only two avalanches of similar size and type. Nevertheless, the observed dependence of deposit depth on slope angle will occur for any material with a yield stress. Thus, our results should have considerable generality. This is also suggested by the strong similarity with the Pouliquen model, even though this was developed using a completely different material and on a considerably smaller scale. Since our data are only for dry avalanches we could not prove that similar results would also hold true for wet avalanches, but since cohesive forces are stronger in wet snow than in dry snow we expect that similar results will hold.

[62] Our observations may also be useful for investigating other gravity-driven flows of materials with yield stresses. These include rockslides, landslides, and some types of mudflow and pyroclastic flow. It would be very interesting to see if similar relations between deposit thickness and slope angle hold in these flows, particularly since in these cases the deposit can exist for a long time after the event. Thus, our approach may be useful for interpreting deposit data from many geophysical flows.

[63] **Acknowledgments.** Parts of this work have been funded by the Swiss National Foundation under grant 206021-113069/1. We thank F. Dufour for organization of field campaigns, P. Bartelt for interesting discussions, and the Canton Valais, Switzerland, for the important financial support. J.N.M. was supported by the Engineering and Physical Sciences Research Council, and his visits to Davos were supported by the Royal Society and the Swiss National Science Foundation.

References

Ammann, W. J. (1999), A new Swiss test-site for avalanche experiments in the Vallée de la Sionne/Valais, *Cold Reg. Sci. Technol.*, *30*, 3–11.

Bartelt, P., and B. W. McArdell (2009), Granulometric investigations of snow avalanches, *J. Glaciol.*, *55*(193), 829–833.

Félix, G., and N. Thomas (2004), Relation between dry granular flow regimes and morphology of deposits: Formation of levées in pyroclastic deposits, *Earth Planet. Sci. Lett.*, *221*, 197–213.

Gauer, P., and D. Issler (2004), Possible erosion mechanisms in snow avalanches, *Ann. Glaciol.*, *38*, 384–392.

Gray, J. M. N. T., Y.-C. Tai, and S. Noelle (2003), Shock waves, dead zones and particle-free regions in rapid granular free-surface flows, *J. Fluid Mech.*, *491*, 161–181.

Gubler, H., and M. Hiller (1984), The use of microwave FMCW radar in snow and avalanche research, *Cold Reg. Sci. Technol.*, *9*, 109–119.

Issler, D. (1999), European avalanche test sites: Overview and analysis in view of coordinated experiments, *Rep. 59*, Eidg. Inst. fuer Schnee und Lawinenforsch., Davos, Switzerland.

Issler, D. (2003), Experimental information on the dynamics of dry-snow avalanches, in *Dynamic Response of Granular and Porous Materials Under Large and Catastrophic Deformations*, *Lecture Notes Appl. Comput. Mech.*, vol. 11, edited by K. Hutter and N. Kirchner, pp. 109–160, Springer, Berlin.

Jenkins, J. T. (2006), Dense shearing flows of inelastic disks, *Phys. Fluids*, *18*, 103307, doi:10.1063/1.2364168.

Jop, P., Y. Forterre, and O. Pouliquen (2006), A constitutive law for dense granular flows, *Nature*, *441*, 727–730, doi:10.1038/nature04801.

Kern, M. A., F. Tiefenbacher, and J. N. McElwaine (2004), The rheology of snow in large chute flows, *Cold Reg. Sci. Technol.*, *39*, 181–192.

Kern, M. A., P. Bartelt, B. Sovilla, and O. Buser (2009), Measured shear rates in large dry and wet snow avalanches, *J. Glaciol.*, *55*(190), 327–338.

Kneller, B., and C. Buckee (2000), The structure and fluid mechanics of turbidity currents: A review of some recent studies and their geological implications, *Sedimentology*, *47*, 62–94.

Louge, M. Y., R. Steiner, S. Keast, R. Decker, J. Dent, and M. Schneebeli (1997), Application of capacitance instrumentation to the measurement of density and velocity of flowing snow, *Cold Reg. Sci. Technol.*, *25*, 47–63.

Martinez-Vazquez, A., and J. Fortuny-Guasch (2006), 3 winters of snow monitoring with the LISA instrument in the Sion valley (CH): 2003–2006 [DVD], *Rep. EUR 22533 EN*, Eur. Comm., Luxembourg.

McElwaine, J. N., and B. Turnbull (2005), Air pressure data from the Vallée de la Sionne avalanches of 2004, *J. Geophys. Res.*, *110*, F03010, doi:10.1029/2004JF000237.

Naaim, M., T. Faug, and F. Naaim-Bouvet (2003), Dry granular flow modelling including erosion and deposition, *Surv. Geophys.*, *24*, 569–585.

Platzer, K., P. Bartelt, and M. Kern (2007), Measurements of dense snow avalanche basal shear to normal stress ratios (S/N), *Geophys. Res. Lett.*, *34*, L07501, doi:10.1029/2006GL028670.

Pouliquen, O. (1999), Scaling laws in granular flows down rough inclined planes, *Phys. Fluids*, *11*, 542–548.

Rammer, L., M. Kern, U. Gruber, and F. Tiefenbacher (2007), Comparison of avalanche-velocity measurements by means of pulsed Doppler radar, continuous wave radar and optical methods, *Cold Reg. Sci. Technol.*, *50*, 35–54, doi:10.1016/j.coldregions.2007.03.014.

Sovilla, B., F. Sommavilla, and A. Tomaselli (2001), Measurements of mass balance in dense snow avalanche events, *Ann. Glaciol.*, *32*, 230–236.

Sovilla, B., P. Burlando, and P. Bartelt (2006), Field experiments and numerical modeling of mass entrainment in snow avalanches, *J. Geophys. Res.*, *111*, F03007, doi:10.1029/2005JF000391.

Sovilla, B., M. Schaer, M. Kern, and P. Bartelt (2008a), Impact pressures and flow regimes in dense snow avalanches observed at the Vallée de la Sionne test site, *J. Geophys. Res.*, *113*, F01010, doi:10.1029/2006JF000688.

Sovilla, B., M. Schaer, and L. Rammer (2008b), Measurements and analysis of full-scale avalanche impact pressure at the Vallée de la Sionne test site, *Cold Reg. Sci. Technol.*, *51*, 122–137, doi:10.1016/j.coldregions.2007.05.006.

Tai, Y. C., and C. Y. Kuo (2008), A new model of granular flows over general topography with erosion and deposition, *Acta Mech.*, *199*, 71–96.

Tiefenbacher, F., and M. A. Kern (2004), Experimental devices to determine snow avalanche basal friction and velocity profiles, *Cold Reg. Sci. Technol.*, *38*, 17–30.

Vallet, J., U. Gruber, and F. Dufour (2001), Photogrammetric avalanche volume measurements at Vallée de la Sionne, Switzerland, *Ann. Glaciol.*, *32*, 141–146.

Vallet, J., B. Turnbull, S. Joly, and F. Dufour (2004), Observations on powder snow avalanches using videogrammetry, *Cold Reg. Sci. Technol.*, *39*, 153–159.

Vilajosana, I., G. Khazaradze, E. Suriñach, E. Lied, and K. Kristensen (2007), Snow avalanche speed determination using seismic methods, *Cold Reg. Sci. Technol.*, *49*, 2–10.

J. N. McElwaine, Department of Applied Mathematics and Theoretical Physics, University of Cambridge, Cambridge, CB3 0WA, UK.

M. Schaer and B. Sovilla, WSL Institute for Snow and Avalanche Research SLF, Flüelastr. 11, CH-7260 Davos Dorf, Switzerland. (sovilla@slf.ch)

J. Vallet, Ulrich, Wiesmann and Rolle, Le Grand-Chemin 73, CH-1066 Epalinges, Switzerland.